



**HAL**  
open science

## Investigation of magnetic field signals during vortex-induced pressure drops at InSight

Shea N. Thorne, Catherine L. Johnson, Anna Mittelholz, Benoît Langlais,  
Ralph Lorenz, Naomi Murdoch, Aymeric Spiga, Suzanne E. Smrekar, W.  
Bruce Banerdt

► **To cite this version:**

Shea N. Thorne, Catherine L. Johnson, Anna Mittelholz, Benoît Langlais, Ralph Lorenz, et al..  
Investigation of magnetic field signals during vortex-induced pressure drops at InSight. *Planetary and  
Space Science*, 2022, 217, pp.105487. 10.1016/j.pss.2022.105487 . insu-03682334

**HAL Id: insu-03682334**

**<https://insu.hal.science/insu-03682334>**

Submitted on 14 Oct 2022

**HAL** is a multi-disciplinary open access archive for the deposit and dissemination of scientific research documents, whether they are published or not. The documents may come from teaching and research institutions in France or abroad, or from public or private research centers.

L'archive ouverte pluridisciplinaire **HAL**, est destinée au dépôt et à la diffusion de documents scientifiques de niveau recherche, publiés ou non, émanant des établissements d'enseignement et de recherche français ou étrangers, des laboratoires publics ou privés.

# Investigation of Magnetic Field Signals During Vortex-Induced Pressure Drops at InSight

## List of Authors:

Shea N. Thorne<sup>1</sup>, Catherine L. Johnson<sup>1,2</sup>, Anna Mittelholz<sup>3</sup>, Benoit Langlais<sup>4</sup>, Ralph Lorenz<sup>5</sup>, Naomi Murdoch<sup>6</sup>, Aymeric Spiga<sup>7,8</sup>, Suzanne E. Smrekar<sup>9</sup>, W. Bruce Banerdt<sup>9</sup>

## Affiliations:

<sup>1</sup>Department of Earth, Ocean and Atmospheric Sciences, The University of British Columbia, Vancouver, Canada.

<sup>2</sup>Planetary Science Institute, Tucson, Arizona, USA.

<sup>3</sup>Department of Earth and Planetary Sciences, Harvard University, Cambridge, MA, USA.

<sup>4</sup>Laboratoire de Planétologie et Géosciences, UMR 6112, Nantes Université, Université d'Angers, Le Mans Université, CNRS, Nantes, France.

<sup>5</sup>Johns Hopkins Applied Physics Laboratory, Laurel, MD, USA.

<sup>6</sup>ISAE-SUPAERO, Université de Toulouse, Toulouse, France.

<sup>7</sup>Laboratoire de Météorologie Dynamique/Institut Pierre-Simon Laplace, Sorbonne Université, Centre National de la Recherche Scientifique, École Polytechnique, École Normale Supérieure, Campus Pierre et Marie Curie BC99, Paris, France.

<sup>8</sup>Institut Universitaire de France, Paris, France.

<sup>9</sup>Jet Propulsion Laboratory, California Institute of Technology, Pasadena, CA, USA

Corresponding author: Shea Thorne (sthorne@eoas.ubc.ca, 302 Earth and Oceans Science 6339 Stores Road V6T 1Z4 Vancouver, BC, Canada)

## Abstract

The NASA InSight lander has recorded many pressure drops attributed to convective vortices during its first full year of data collection. However, although dust-carrying vortices (dust devils) are a common phenomenon on Mars, they have not been observed in InSight images. On Earth, magnetic signals associated with some dust devils have been reported. Data from the InSight Fluxgate Magnetometer (IFG) provide the first opportunity for similar investigations on Mars. Here, we evaluate whether magnetic signals are associated with daytime vortices. We incorporate observations of environmental conditions, measurements of ground tilt from seismic data, and data from the lander's solar panels, and consider the potential for dust-laden vortices to generate observable magnetic field signals. We find that 7.7% of pressure drop events greater than 1 Pa show a resolvable magnetic field signal at the time of the pressure drops. The resolvable magnetic signals, typically seen on the horizontal field components, are less than 1 nT in amplitude, and have no clear correlation with local time, duration, or pressure drop magnitude. During nine pressure drop events we found smoothly varying magnetic signals of at least 0.3 nT on any one component. To investigate the origin of these magnetic signals we evaluated three possible sources: solar array currents, ground and lander tilt, and triboelectric effects of lofted dust. We find that SAC and tilt could contribute a change in the magnetic field but cannot solely explain the observed signals. The observed changes in field strength could theoretically be produced via triboelectric effects, but only in the case of exceptionally large dust devils that pass close to the lander. The lack of imaged dust devils and the small number of observed magnetic signatures despite numerous measured pressure drops is consistent with at most a small

46 proportion of dust laden convective vortices at InSight and associated predicted triboelectric  
47 effects.

48

49 Keywords: Dust devils, Convective vortices, Magnetic Fields, Mars, InSight, Triboelectricity

50

## 51 1 Introduction

52 The Interior Exploration using Seismic Investigations, Geodesy and Heat Transport (InSight)

53 Mars Lander touched down on November 26, 2018 in Elysium Planitia. It carries the Auxiliary

54 Payload Sensor Suite (APSS) that includes the InSight FluxGate magnetometer (IFG). The IFG is

55 the first magnetometer on the surface of Mars, and thus provides a unique opportunity to study

56 the static crustal and time-varying external magnetic fields below the martian ionosphere

57 (Banfield et al., 2018). To date, the crustal magnetic field strength,  $\sim 2000$  nT, and direction as

58 well as diurnal magnetic field variations measured by the IFG have been investigated (Banerdt et

59 al., 2020; Johnson et al., 2020; Mittelholz et al., 2020). However, the IFG has also measured

60 aperiodic magnetic signals that occur over timescales of seconds to minutes. Here we use IFG

61 data, together with observations of environmental conditions around the lander by APSS

62 (Banfield et al., 2018), measurements of ground tilt from seismic data, and data from the

63 InSight's solar panels, to evaluate whether magnetic signals are associated with daytime

64 convective vortices. Of specific interest is whether potentially dust-laden convective vortices,

65 i.e., dust devils, generate observable magnetic field signals at the InSight landing site.

66 Dust devils (DDs) were first observed on Mars in Viking Orbiter images and have been

67 subsequently imaged by many missions, either via direct imaging or by the tracks left from the

68 passage of DDs (Balme & Greeley, 2006; Thomas & Gierasch, 1985). Martian DDs provide an

69 important mechanism for dust injection into the atmosphere (Kahre, Murphy, & Haberle, 2006)

70 as well as for the vertical transport of heat (Renno et al. 2004), and have been proposed to

71 maintain current flow among atmospheric regions (Harrison et al., 2016). DDs also contribute to

72 global atmospheric conditions via their effects on convective circulation and a multi-year study of

73 martian DD heights found that they correlate seasonally with the thickness of the planetary

74 boundary layer, a descriptive measure of the vigor of convective atmospheric activity (Fenton &

75 Lorenz, 2015). The electrification of DDs could also affect martian habitability as they have been

76 purported to induce production of  $H_2O_2$  which could be responsible for scavenging organic

77 material or reducing the residence time of methane gas in the martian atmosphere (Atreya et al.,

78 2006). Although that process has been shown to have limited impact (Kok & Renno, 2009), the

79 electric and magnetic signatures of dusty atmospheric structures need to be better assessed. DDs

80 are specifically important to planetary missions because of the possibility for dust deposition on,

81 or removal from, solar panels that in turn can shorten or extend mission operations, respectively

82 (Lorenz & Reiss, 2015), and their electromagnetic noise has been hypothesized to affect

83 communication equipment (Harrison et al., 2016).

84

85 October 2020 marked a full martian year of data collection by the pressure sensor instrument on

86 InSight, providing a set of 11,251 pressure drops which were recently compiled (Spiga et al.,

87 2021; Chatain, Spiga, et. al. 2021). The InSight landing site is the most active site for vortices of

88 all landed martian missions to date (Banerdt et al., 2020). Convective vortices are classified as

89 DDs if they loft dust, but the fraction of DDs to dustless vortices is not well understood (Lorenz

90 & Jackson, 2015; Spiga et al., 2016). To date InSight has not imaged any DDs despite targeted

91 surveys (Banfield et al., 2020; Lorenz, Spiga, et al., 2021) but DD tracks around the lander have

92 been observed via satellite imagery (Perrin et al., 2020) and by InSight's cameras (Charalambous  
93 et al., 2021). A recent study of parameters inferred for a subset of these vortices together with  
94 advective wind speeds suggests that high wind speeds at the InSight landing site may suppress  
95 the formation of DDs (Jackson et al., 2021).

96  
97 The uplift of a passing vortex is known to also affect seismic measurements (Lorenz et al.,  
98 2015). InSight's Seismic Experiment for Interior Structure (SEIS) instrument and the pressure  
99 sensor have observed simultaneous seismic and pressure signals due to convective vortices  
100 (Lognonné et al., 2020, Murdoch et al., 2021). One such observation also corresponds to a  
101 newly-formed DD track that came within 19 m of the lander, and the track was imaged from the  
102 lander's camera and from orbit (Banerdt et al., 2020). These joint observations permitted  
103 estimates of the vortex properties (e.g., diameter), as well as the elastic rigidity (compliance) of  
104 the ground near the landing site.

105  
106 On Earth, there have been two observations of magnetic signals from dust carrying vortices in  
107 the form of ultra-low frequency electromagnetic emission in conjunction with the passage of a  
108 DD, at distances up to 100's of meters from the electromagnetic sensors (Farrell et al., 2004;  
109 Houser, Farrell, & Metzger, 2003). The first such DD, reported by Houser et al. (2003) was  
110 approximately 10 meters wide and 200 meters tall with continuous broadband electromagnetic  
111 emission at frequencies below 50 Hz with peaks near 10 Hz, while the second reported by Farrell  
112 et al., 2004 again detected magnetic emission between 1-10 Hz (see further Figures 3 and 4 in  
113 Farrell et al., 2004), reporting a magnetic field of  $\sim 0.1$  nT immediately outside the DD. One  
114 possible origin for the magnetic field signals, discussed in the terrestrial literature is  
115 cyclostrophic motion of triboelectrically charged lofted dust, behaving as a magnetic solenoid  
116 (Farrell et al., 2006; Kurgansky, Baez, & Ovalle, 2007).

117  
118 In this study we look for possible DD signatures in the magnetic field measurements recorded by  
119 InSight. Assuming they can be tied to other meteorological information, they could help  
120 constrain the subset of the convective vortices that are DDs (Houser et al., 2003). A few pressure  
121 drop events have been found to exhibit magnetic signals; however the origin of these was unclear  
122 (Charalambous et al., 2021; Johnson et al., 2020). A passing vortex, if a DD, could be observed  
123 in IFG data via one or more of the following possible mechanisms: (1) Triboelectrically charged  
124 lofted dust, as suggested for terrestrial DD magnetic emission (Farrell et al., 2006; Kurgansky,  
125 Baez, & Ovalle, 2007), (2) Changing solar array currents as a result of entrained dust of a  
126 passing DD obscuring the solar arrays (as observed at InSight during transits of Phobos (Stähler  
127 et al., 2020), (3) Ground tilting resulting from the pressure lows at the center of convective  
128 vortices (Lognonné et al., 2020, Murdoch et al., 2021) that changes the orientation of the IFG in  
129 the ambient crustal magnetic field, and (4) similarly, wind-induced tilt of the lander as explored  
130 previously for the seismometer on the lander deck (Murdoch et al, 2017, Panning et al., 2020).  
131 The goal is therefore to establish, if, when, and why pressure drops at the InSight lander have  
132 associated magnetic signals and in particular to evaluate whether any such signals can be  
133 attributed to DDs. Here, we first identify the fraction of pressure drop events that have a  
134 resolvable magnetic signature. These resolvable events and their characteristics are then used to  
135 evaluate the four mechanisms through which a vortex or DD could create a magnetic signal.

136

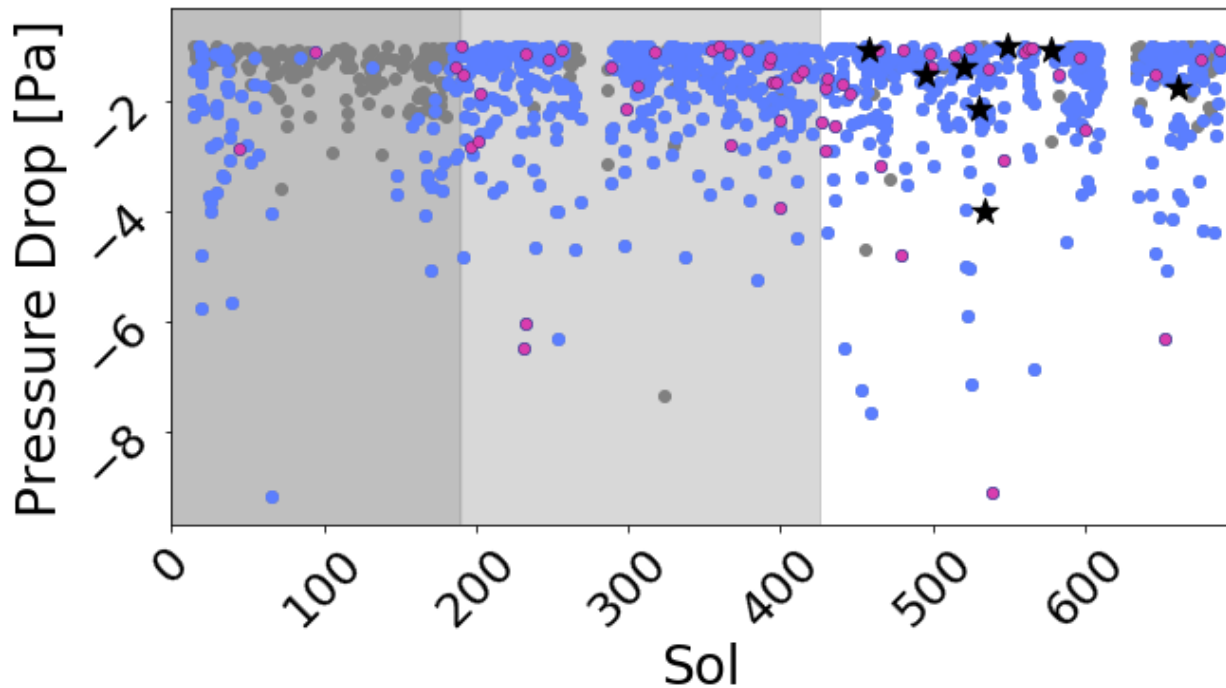
## 137 2 Resolvable Magnetic Signatures at the Times of Pressure Drops

## 138 2.1 IFG Data during pressure drops

139 From the set of 11,251 pressure drops over the first martian year of InSight data collection  
 140 (Spiga et al., 2021; Chatain, Spiga, et. al. 2021), we selected the 1061 events that exhibit  
 141 pressure drops of at least 1 Pa (Figure 1). This excludes small events unlikely to loft dust  
 142 (Lorenz, Spiga, et al., 2021).

143

144



145

146 **Figure 1.** 1061 pressure drops greater than 1 Pa recorded by InSight during the first full Martian  
 147 year of observations. At sol 189 the IFG sampling rate for continuous data increased from 0.2 Hz  
 148 to 2 Hz (dark gray to light gray background transition) and at sol 426 the solar array current  
 149 cadence increased from 0.0167 Hz to 0.25 Hz when recorded (light gray background to white  
 150 background). All events (gray), events with either continuous 2 Hz IFG data or 20 Hz data down-  
 151 sampled to 2 Hz (blue,  $N = 862$ ), events with a standard deviation signal to noise ratio ( $SNR_{\sigma} \geq$   
 152 2 (pink,  $N = 66$ ), and the subset ( $N = 8$ ) of  $SNR_{\sigma} \geq 2$  events with 0.25 Hz solar array current data  
 153 (black stars).

154

155 The continuous sampling rate of the IFG was initially 0.2 Hz, and on sol 189 it was increased to  
 156 2 Hz. For short timeframes of interest 20 Hz data can be requested and these are available for  
 157 some of the observed pressure drop times. Intermittent outages of the data acquisition electronics  
 158 for IFG (the Payload Auxiliary Electronics (PAE)) resulted in data gaps in the IFG and other  
 159 meteorological sensor data sets. For one 10-day interval, sols 261 – 269, the continuous sampling  
 160 rate was decreased again to 0.2 Hz because of downlink limitations just before solar conjunction  
 161 and a spacecraft anomaly (sols 270 – 283) led to a subsequent data gap until communication with  
 162 the spacecraft could be resumed. Further PAE anomalies occurred but were mostly addressed  
 163 within a time frame of a few hours.

164

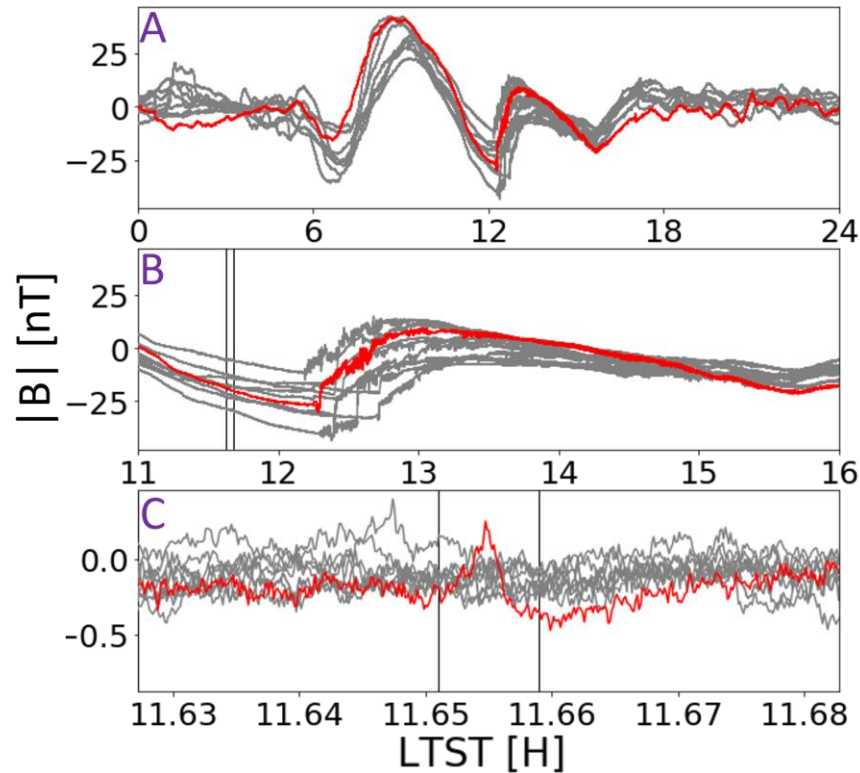
165 We initially used 0.2 Hz data (recorded or decimated from higher frequency data) to assess the  
166 overall shape and structure of magnetic signals at the times of the pressure drops (e.g., Figure 2),  
167 but found they lacked sufficient temporal resolution to characterize the magnetic field in detail  
168 during pressure drops. Therefore, we retained 879 events for which either 2 Hz or 20 Hz data  
169 (V6; Joy et al., 2019) were available, and the 20 Hz data were down-sampled to 2 Hz to create a  
170 consistent data set, using the same approach applied to the IFG data set (Joy et al., 2019). We  
171 inspected these 879 events by hand to identify any magnetic signals of artificial origin, i.e.,  
172 lander activities, at the times of pressure drops. Such activities include the lander wake on/off  
173 commands, communications, or movement of the lander's robotic arm, all of which generate  
174 magnetic signals that are not completely removed from the calibrated IFG data (Johnson et al.,  
175 2020; Mittelholz et al., 2020; Thorne et al., 2020). 17 events had magnetic field signals with  
176 clear artificial origins and were discarded, resulting in a final set of 862 events. Magnetic field  
177 components are reported in the InSight lander level coordinate system in which X points north,  
178 Y points east and Z points down (Johnson et al., 2020; Joy et al., 2019).

179

## 180 2.2 Event Identification and Resulting Statistics

181 Mars exhibits diurnal magnetic field changes as well as shorter period variations throughout a sol  
182 (Mittelholz et al., 2020). As an example, we show the magnetic field for sols 529 – 539 (Figure  
183 2); on one of these sols (534) a pressure drop with a resolvable magnetic field signal is seen  
184 (Figure 2C, discussed more below). As discussed in Mittelholz et al. (2020), the diurnal cycle  
185 (Figure 2A) has a peak in the early to mid-morning. This is attributable, at least in part, to wind-  
186 driven ionospheric currents that in turn depend on atmospheric properties such as horizontal  
187 wind speed and electron density (see review in Mittelholz et al., 2020). Increased noise in the  
188 data is clearly seen on all sols between ~11:00 – 16:00 hrs, and this is inferred to result from  
189 short time-scale variability in solar array currents (Johnson et al., 2020). Although the example  
190 event occurs during a comparably "quiet" time (Figure 2A,B), during the event time frame  
191 (Figure 2C) the background noise is substantial, requiring care in identifying any magnetic  
192 signature of pressure drop events.

193



194  
195

196 **Figure 2.** IFG magnitude  $|B|$ , detrended over a full sol, plotted for 10 sols (529-539) with sol  
197 534 (red), on which a convective vortex studied here occurs. (a)  $|B|$  over a full sol. (b) LTST  
198 ~11:00-16:00 with the time of event on sol 534 plotted in Figure 4A identified by vertical lines.  
199 (c)  $|B|$  during the corresponding LTST for which an event was detected on sol 534 (shown in  
200 Figure 4A), detrended over the time window shown to highlight the noise. Vertical lines show the  
201 duration of the event (28.8 seconds).

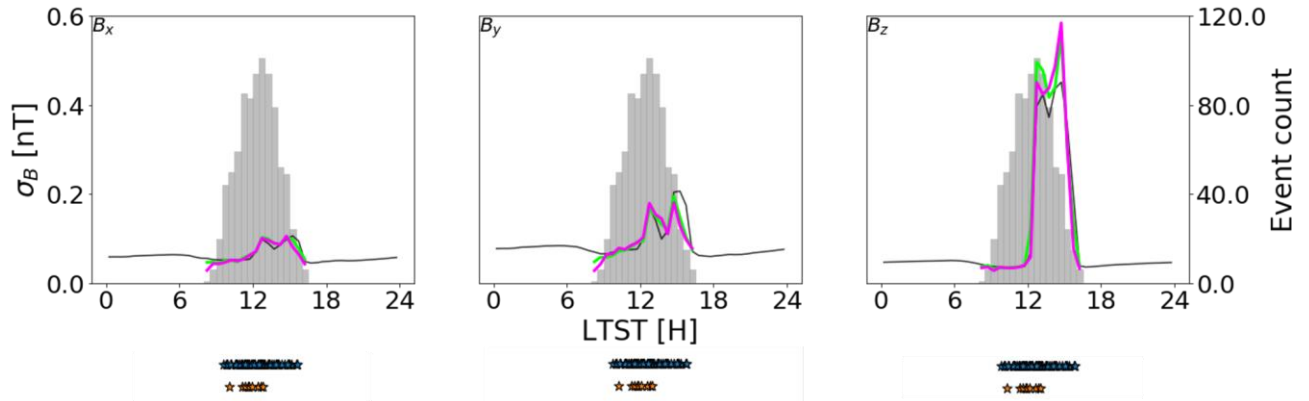
202

203 We first assessed the typical variability in the field over the characteristic timescale of pressure  
204 drops at all local times (Figure 3). We compared this with the local magnetic field variability  
205 immediately before and after each of the 862 events, as well as with the variability during a  
206 pressure drop to assess whether magnetic signatures during the times of pressure drops can be  
207 distinguished from background fluctuations.

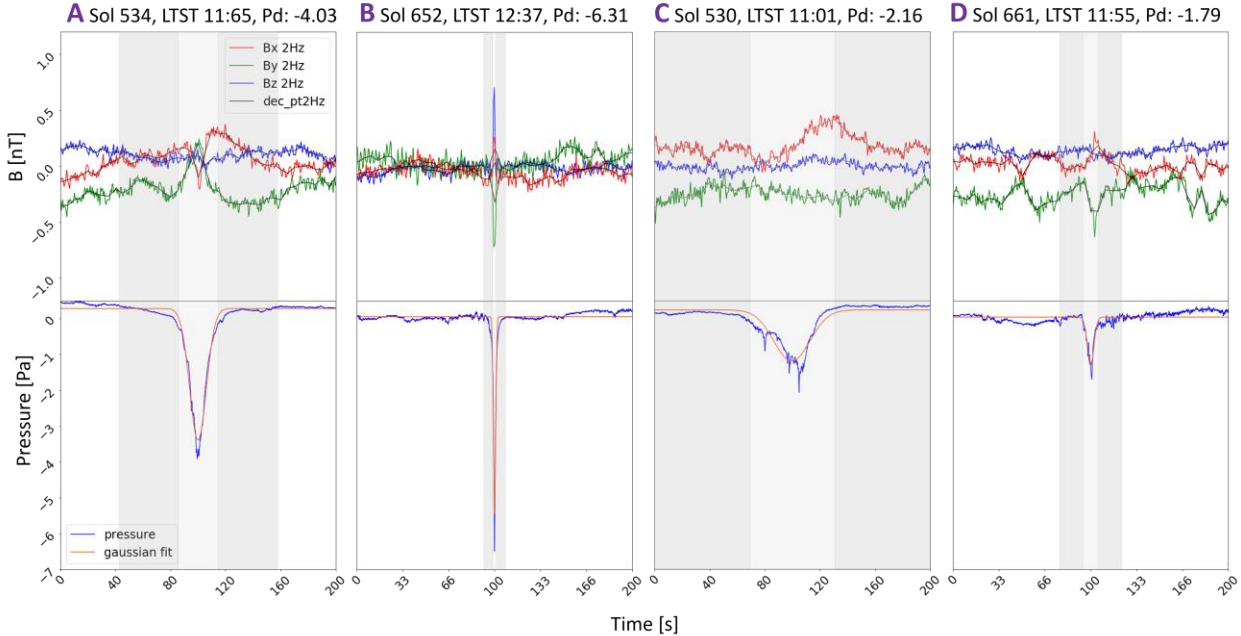
208

209 Pressure drop durations (twice the full-width-at-half-max, FWHM) were obtained via gaussian  
210 fitting of a 200 second interval of detrended pressure data centered on the pressure drop peak,  
211 following the methodology described in Murdoch et al. (2021). To capture the typical  
212 background variability in the field on the time scale of pressure drops, each sol with 2 Hz data  
213 first had a 60s running mean removed and was then divided into sections the length of the  
214 average duration of pressure drop events (21.7 seconds). The standard deviation ( $\sigma$ ) in each field  
215 component for each section was computed, binned into half hour local time bins, and the median  
216 value of  $\sigma$  in each bin was computed (Figure 3). For pressure drop events, the local background  
217 variability in each magnetic field component was quantified by the average  $\sigma$  of the magnetic  
218 field in windows 1.5 times the duration of the individual event, directly before and after the

219 pressure drop ( $\sigma^{\text{bk}}$ ) (the dark grey shading in Figure 4). The magnetic field variability during  
 220 each event was characterized by the  $\sigma$  during the pressure drop ( $\sigma^{\text{pd}}$ ) (the light grey shading in  
 221 Figure 4).  
 222



223  
 224 **Figure 3.** Median standard deviation in each magnetic field component,  $\sigma$ , during (pink) and  
 225 directly surrounding (green) pressure drop events, as well as the ambient variability in the field  
 226 over the characteristic time scale of a pressure drop (black), all shown for the first year of the  
 227 mission and binned in 30 min local true solar time (LTST) bins. The number of pressure drop  
 228 events per bin is shown by gray bars. Blue stars are plotted below the x-axis at the local time for  
 229 each of the 66 events with a  $\text{SNR}_\sigma \geq 2$  in at least one magnetic field component. Orange stars  
 230 show the 9 events highlighted in section 2.3.  
 231



232  
 233  
 234 **Figure 4.** A-D show 4 examples of pressure drop events with sol number, local time of pressure  
 235 drop peak, and pressure drop (Pd) in Pa identified by Spiga et al., 2021. Top row: North ( $B_x$  -  
 236 Red), East ( $B_y$  - Green) and Vertical Down ( $B_z$  - Blue) magnetic field components during each  
 237 pressure drop (light grey shading) and the surrounding background period (darker grey shading,

238 *1.5 times the event duration before and after the event). 2 Hz (colors) and decimated 0.2 Hz*  
 239 *(blackline) data after subtraction of a 60s moving average are shown. Bottom row: pressure*  
 240 *drop (blue) with gaussian fit (red). A and D have  $SNR_{\sigma} > 2$  and  $SNR_{P2P} > 1.8$  in the  $B_Y$*   
 241 *component, B has  $SNR_{\sigma}$  and  $SNR_{P2P}$  above their respective thresholds in all 3 components, and*  
 242 *C has  $SNR_{\sigma} > 2$  in  $B_Y$ .*

243

244 Overall, the variability in the ambient magnetic field increases substantially between noon and  
 245 4pm local true solar time on each sol (Figures 2,3). This is in part related to varying current  
 246 draws from the solar array panels and other lander activities (Johnson et al., 2020; Mittelholz et  
 247 al., 2020; Lorenz et al., 2020). The  $\sigma$  immediately before and after an event, as well as during an  
 248 event, are similar in amplitude to the typical variability in the field. This suggests that, on  
 249 average, magnetic signals at times of pressure drops are not significantly different from those in  
 250 the immediate surrounding intervals or the typical background variability at that local time.  
 251 Furthermore, the typical variability in the vertical magnetic field component is much larger than  
 252 on the horizontal channels, typical  $\sim 0.5$  nT between noon and 4pm LTST. This analysis also  
 253 shows that identification of signals in the IFG data is not trivial due to typical short-term  
 254 variability in the data.

255

256 As we had no a priori expectations as to how a DD might manifest in the IFG data, we used two  
 257 methods to quantify the signals during individual events. We first determined the signal to noise  
 258 ratio (SNR) for each of the 862 events to systematically identify those with a resolvable  
 259 magnetic signature. The signal for each event, as identified in the pressure data, was detrended  
 260 with a 60 second running mean (described above), to remove longer time scale variations  
 261 unassociated with the pressure drop. We defined the standard deviation signal to noise ratio  
 262  $SNR_{\sigma}$  as the ratio  $\sigma^{pd} / \sigma^{bk}$ . We found that 66 of the 862 events recorded at 2 Hz had a  $SNR_{\sigma}$   
 263 greater than or equal to 2 on at least one magnetic field component (Figure 1).

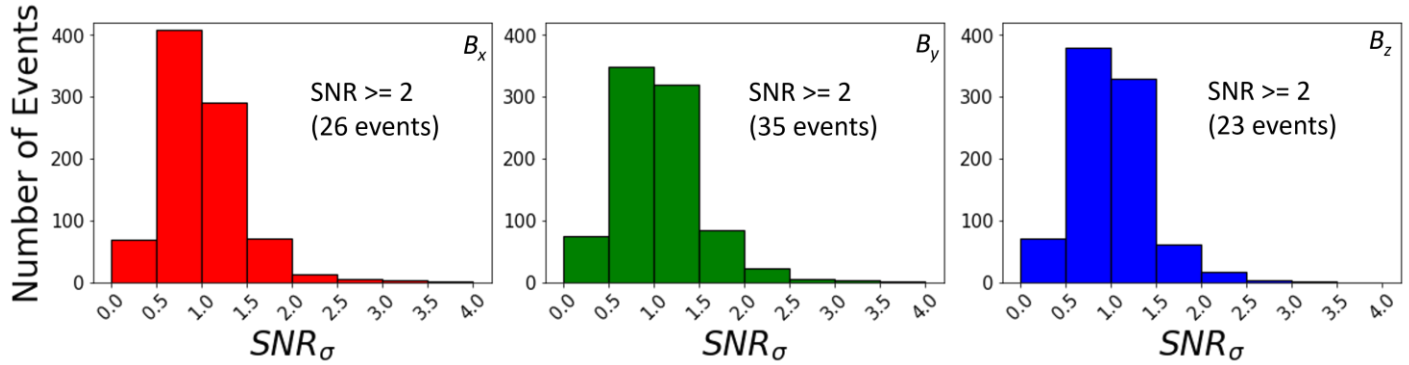
264

265 We also implemented a selection scheme in which we replaced  $\sigma^{pd}$  and  $\sigma^{bk}$  with the maximum  
 266 excursion (i.e., the range or peak-to-peak amplitude) during and before/after the event  
 267 respectively and recomputed the SNR using these values, termed the  $SNR_{P2P}$ . We found that this  
 268 method systematically resulted in the detection of fewer high SNR events c.f. the standard  
 269 deviation approach. To compare whether the two approaches identified similar populations of  
 270 events we first plotted empirical cumulative distribution functions for  $SNR_{P2P}$  and  $SNR_{\sigma}$  (for each  
 271 component). We used these to determine the  $SNR_{P2P}$  value that corresponds to the same number  
 272 of events with resolvable magnetic field signals as identified using a  $SNR_{\sigma} = 2$ . This resulted in a  
 273  $SNR_{P2P} = 1.8$ . We found that 46 of the 66 events (70%) identified using the  $SNR_{\sigma} = 2$  were also  
 274 identified using  $SNR_{P2P} = 1.8$  indicating substantial, but not complete, overlap in the populations  
 275 (see details in Supplementary Table 1 and Catalogue). Although the  $SNR_{P2P}$  might seem a more  
 276 obvious approach, noise in the IFG data can result in spurious range measurements and is more  
 277 sensitive to outliers. We thus chose to use the events identified using  $SNR_{\sigma}$  for further analyses.  
 278 Examples for three events are shown in Figure 4, and all events identified with either the  
 279 standard deviation or range approach are catalogued in the Supplemental Information.

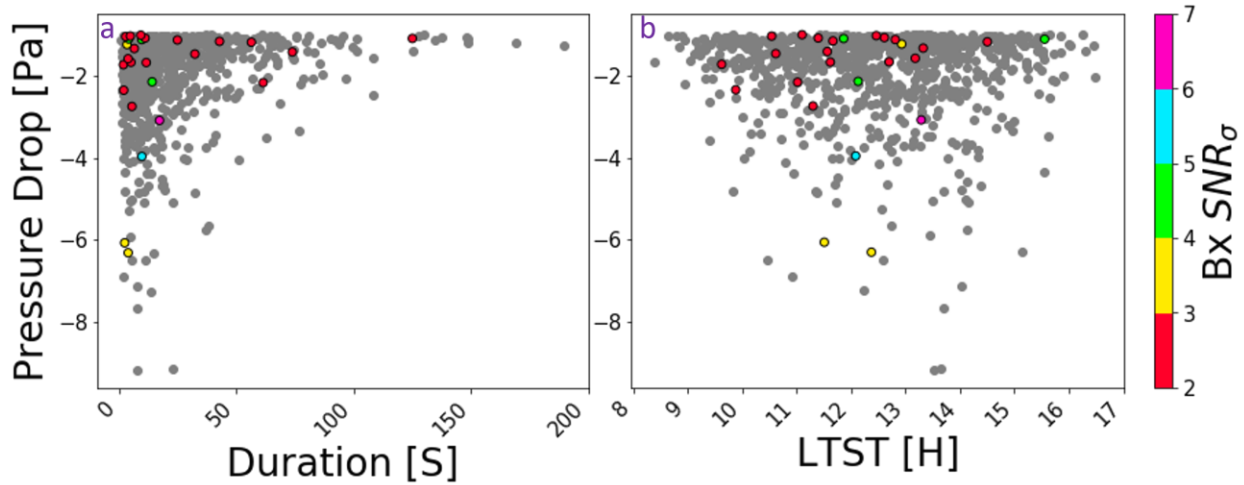
280

281 The 66 high  $SNR_{\sigma}$  events correspond to 6.2% of all pressure drops  $> 1$  Pa and 7.7% of the 862  
 282 events with IFG data. In detail, we find that for most events only one magnetic field component  
 283 has a  $SNR_{\sigma} \geq 2$ . For  $B_X$ ,  $B_Y$ , and  $B_Z$  this occurred for 3.0% (N=26), 4.1% (N=35), and 2.7%

284 (N=23) of the 862 pressure drops respectively (Figure 5). We further observe that resolvable  
 285 events have no clear correlation with local time, duration, and pressure drop magnitude (Figure  
 286 6). The local times of all 66  $SNR_{\sigma}$  events (shown with blue stars in Figure 3) are seen to have a  
 287 similar local time distribution to that of the pressure drop events overall.



288  
 289 **Figure 5.** Histograms of the standard deviation signal-to-noise ratios ( $SNR_{\sigma}$ ) for the north ( $B_x$ ),  
 290 east ( $B_y$ ) and vertical down ( $B_z$ ) magnetic field components. The numbers of events with  $SNR_{\sigma}$   
 291  $\geq 2$  are given. Seven events with  $SNR_{\sigma} > 4$  are not shown (2 in  $B_x$ , 2 in  $B_y$  and 3 in  $B_z$ ).  
 292

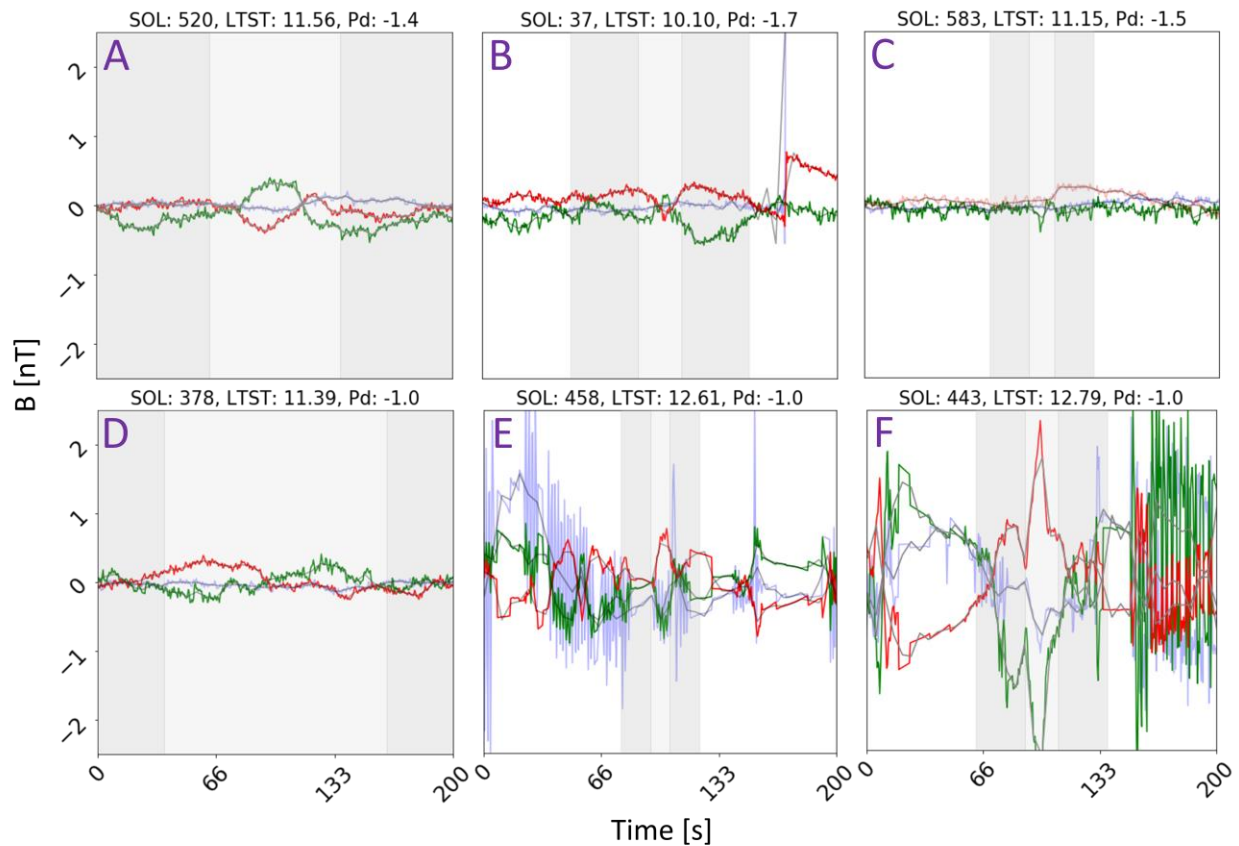


293  
 294 **Figure 6.** Pressure drop magnitude for events with  $SNR_{\sigma} \geq 2$  in the  $B_x$  magnetic field  
 295 component (colored dots), compared with the overall population of pressure drops greater than  
 296 1 Pa examined here. Pressure drop versus (a) event duration (2 x FWHM), and (b) local true  
 297 solar time (LTST). The results for events with  $SNR_{\sigma} \geq 2$  in  $B_y$  and  $B_z$  are similar.  
 298

299 We evaluated whether this occurrence rate of high  $SNR_{\sigma}$  events occurs randomly in the IFG data  
 300 set as follows. For every sol over the martian year with 2 Hz IFG, we computed a  $SNR_{\sigma}$  for local  
 301 time sections of the sol with the length of the average duration of pressure drop events, by  
 302 dividing the  $\sigma$  during the short section by the average  $\sigma$  of the sections before and after it. We  
 303 found that for  $B_x$ ,  $B_y$ , and  $B_z$ , a  $SNR_{\sigma} \geq 2$  occurred for 2.5%, 2.0%, and 2.3% of the 469808  
 304 segments, less than the occurrence rate of a  $SNR_{\sigma} \geq 2$  during the times of pressure drops. This  
 305 analysis confirms that our identification of events is statistically significant, and we reject the  
 306 hypothesis that our identifications are not associated with any events.  
 307

308 **2.3 Magnetic Field Signals During Pressure Drops**

309 Our event detection method identified 66 pressure drop events, 8 of which have concurrent solar  
 310 array current data (see Supplementary Figure 1 and Section 3.1). These events are reported  
 311 together with figures and their statistics in the supplementary information catalog which also  
 312 includes the events identified only by the  $\text{SNR}_{\text{P2P}}$  method and all events with pressure drop  
 313 magnitudes  $\geq 3.8$  Pa (123 events total as listed in Supplementary Table 1). The set of resolvable  
 314 events (as identified by both selection methods) and large pressure events was visually examined  
 315 for magnetic signals that varied smoothly during the pressure drop duration while also showing a  
 316 clear peak-to-peak signal of at least 0.3 nT on any one component. We found that only 9 events  
 317 matched these criteria. Three such events are displayed in Figure 4 (A, B, & D) and the  
 318 remaining 6 are shown in Figure 7. For these events, the components that show the smoothly  
 319 varying signals  $> 0.3$  nT during the pressure drop are observed mostly  $B_X$  and  $B_Y$  (consistent with  
 320 the lower noise level on these channels) and have an average peak-to-peak signal of 0.8 nT with  
 321 a maximum observed range of 2.7 nT ( $B_Y$  in Figure 7F).  
 322  
 323



324  
 325

326 **Figure 7.** A-F show  $B_X$  (red),  $B_Y$  (green) and  $B_Z$  (blue) for 6 resolvable events with smoothly  
 327 varying magnetic signals during the pressure drop in one or more component featuring a peak-  
 328 to-peak signal  $> .3$  nT, plotted in the same style as top row of Figure 4. To highlight the  
 329 identified signals, components that did not fit our selection criteria have increased transparency.  
 330 The panels are titled with sol number, local time of pressure drop peak, and pressure drop (Pd)  
 331 in Pa as identified by Spiga et al., 2021.  
 332

333 We consider these 9 events the best candidate examples of magnetic field signals during pressure  
334 drops of the 862 events examined. Figures 7E and 7F show the challenges associated with  
335 identifying signals in noisy IFG data. Although the remaining events with high SNR may contain  
336 resolvable signals, the signals are either  $< \sim 0.1$  nT or they occur during times of noisy magnetic  
337 field measurements as illustrated by Figure 2. As shown in Figure 3, the 9 events cluster in local  
338 time in the early part of the day and before the onset of the typical increase in variability in the  
339 ambient magnetic field. This is in contrast to the local times of all 66 SNR<sub>o</sub> events which have a  
340 similar local time distribution to that of all pressure drop events.

341

### 342 3 Discussion

343 We investigate three possible sources of the resolvable magnetic signals during the times of  
344 pressure drops: solar array currents, ground and lander tilt, and triboelectric effects. We then  
345 synthesize these results drawing on other InSight observations related to dust movement and DD.

346

#### 347 3.1 Solar Array Currents

348 We investigated whether there is a correlation between changes in the solar array currents and  
349 magnetic signals to assess the possibility that a change in current caused by a DD leads to a  
350 change in the magnetic field. This could occur if lofted dust carried by DDs directly reduces  
351 solar incidence on the panels and thus leads to a drop in the current. Alternatively, increases in  
352 the solar array currents are possible as dust within a DD can scatter sunlight onto the arrays  
353 (Lorenz & Jackson, 2015). The effect could occur on either or both solar panels, depending on  
354 the relative orientations of the passing DD, the sun, and the solar panels. The change in solar  
355 array currents could have an attendant signal in the magnetic field measured by the IFG that  
356 together could help discern dust-free vortices from DDs. Drops in solar flux due to obscuration  
357 of solar cells by DDs have been observed on Earth (Lorenz & Jackson, 2015). At InSight,  
358 magnetic signals have been observed at the times of drops in the currents generated by the solar  
359 arrays during the Phobos and Deimos transits and the associated temporary darkening (Stähler et  
360 al., 2020).

361

362 The relevant solar array current (SAC) data for determining insolation are reported via 2  
363 channels, 771 and 791. They indicate insolation on the east and west solar arrays respectively,  
364 the magnitude of which is relayed through currents from each solar array (Lorenz et al., 2020).  
365 Solar array currents were recorded at a sampling interval of  $\sim 30$  seconds until Sol 426, when the  
366 sampling rate was increased to 4 seconds. However, InSight SAC data are only recorded when  
367 the lander is awake, i.e., not continuously (Lorenz et al., 2020) and long gaps in data coverage on  
368 any individual sol are present (see Figure 4 in Mittelholz et al., 2020). Because of the  
369 intermittent SAC data, a model of daily solar array currents generated to fit data gaps is fit to the  
370 data points as discussed in Joy et al. (2019), and interpolated to the cadence of the IFG data to  
371 correct IFG data for solar array currents. As a result, low frequency variations in the currents  
372 drawn by InSight's solar arrays are generally accounted for in the processing of magnetometer  
373 data, but variations on the time scales of pressure drops are not modeled and could contribute to  
374 IFG signals (Joy et al., 2019; Mittelholz et al., 2020).

375

376 To investigate whether the magnetic field at the time of a pressure drop is correlated with solar  
377 array current signals, we required SAC data throughout the pressure drop and corresponding  
378 flanking periods at a high enough cadence to resolve a change in current during the drop. We

379 thus examined pressure drop events with durations greater than or equal to 8 seconds for which  
 380 0.25 Hz SAC data were available (i.e., on or after Sol 426), resulting in 73 events (see Figure 1).  
 381 This threshold for the pressure drop duration excludes the two DD events identified in the  
 382 Lorenz, Lemmon, & Maki, (2021) SAC survey.

383  
 384 Of the 73 pressure drop events that fit the SAC data criteria, only eight of them have magnetic  
 385 field components with a  $\text{SNR}_\sigma \geq 2$  and three of the eight also have a  $\text{SNR}_{\text{P2P}}$  that exceeds the  
 386  $\text{SNR}_{\text{P2P}} = 1.8$  detection threshold (including Supplementary Figure 1C). Of the eight events, the  
 387 magnetic signal is typically observed on only one of the X, Y, or Z IFG components, and not  
 388 consistently on a specific component (the first 8 events listed in Supplementary Table 1). IFG  
 389 signals are observed to be present both with and without concurrent SAC changes  
 390 (Supplementary Figure 1). Additionally, pressure drops with low IFG  $\text{SNR}_\sigma$  (unresolvable) are  
 391 commonly observed with and without SAC dips. We conclude that the SACs cannot be the only  
 392 source of magnetic field signal during pressure drop events.

### 393 394 3.2 Ground or Lander Tilt

#### 395 3.2.1 Ground Tilt

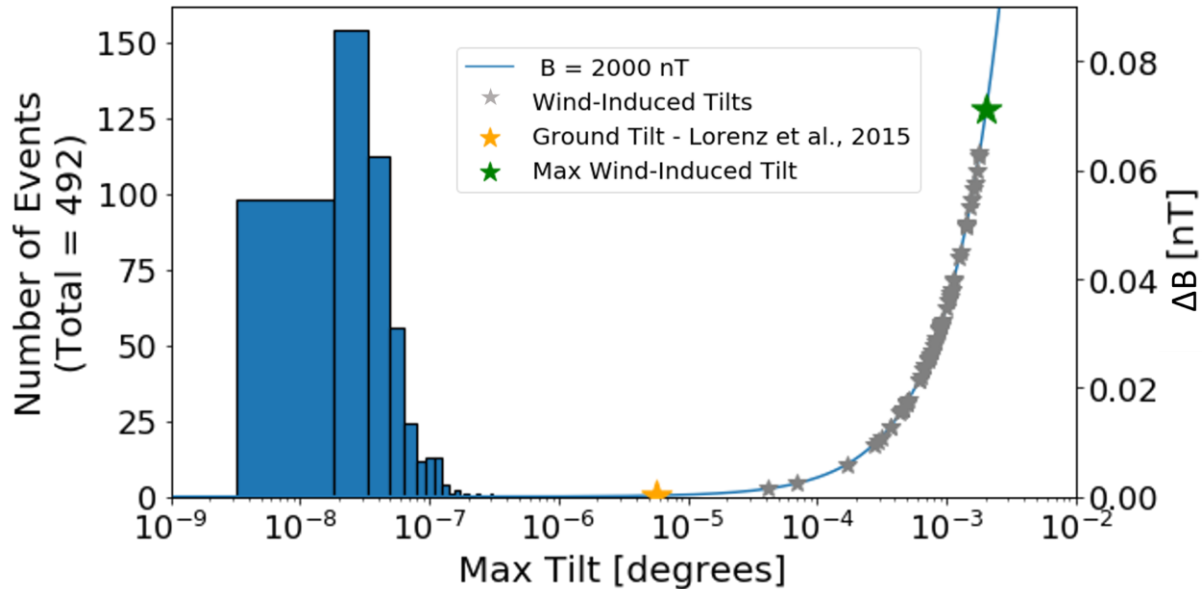
396 Tilting of the InSight lander by ground motion could also be responsible for a change in  
 397 magnetic signal. As a DD or convective vortex is characterized by lower pressure in its center, its  
 398 passage can be observed as the negative load deforms the surface, generating ground tilt  
 399 (Banerdt et al., 2020; Murdoch et al., 2021).

400  
 401 The magnetic signal from a tilt of the lander due to ground motion caused by the low-pressure  
 402 field of a convective vortex can be approximated as a small rotation ( $\alpha$ ) in the magnetometer  
 403 orientation about a horizontal axis in the lander's reference frame. This results in a change in the  
 404 orientation of the IFG with respect to the background crustal magnetic field, producing a change  
 405 in the individual components, but leaving the magnitude of the overall signal unchanged, i.e. the  
 406 new field  $\mathbf{B}' = \mathbf{B} + \Delta\mathbf{B}$ , where  $|\mathbf{B}'| = |\mathbf{B}|$ . Some geometry and algebra yield an expression for  $\Delta B = /$   
 407  $\Delta B /$

$$408 \quad \Delta B = B 4 \sin\left(\frac{\alpha}{4}\right) \cos\left(\frac{\alpha}{4}\right)$$

410  
 411 We calculate values for  $\Delta B$  for ground tilts up to  $10^{-2}$  degrees assuming a surface field strength  $B$   
 412 of 2000 nT at InSight (Johnson et al., 2020; Figure 8). Lorenz et al. (2015) reported terrestrial  
 413 observations of ground tilts of  $\sim 10^{-7}^\circ$  correlated with long period ( $>9$  second) convective  
 414 vortices identified by pressure drops. This terrestrial value, if applicable at Mars, would result in  
 415 a  $\Delta B$  of 0.0002 nT, too small to be resolvable by the IFG. At InSight, seismic observations  
 416 concurrent with pressure drops have been made because the seismometer is able to measure the  
 417 resulting ground deformation (Banerdt et al., 2020; Lognonné et al., 2020; Murdoch et al., 2021).  
 418 Stott et al. (2021) investigated ground tilt during the initial phase of the mission when the  
 419 seismometer was still on the lander deck. They reported a maximum peak-to-peak tilt of  $\sim 0.002^\circ$   
 420 on a three-months timescale, an estimate which captures motion of the regolith and thermoelastic  
 421 tilting of the lander, both expected to be much larger effects than ground tilts during vortex  
 422 events. This is supported by maximum ground tilt magnitudes between  $10^{-9}^\circ$  and  $10^{-6}^\circ$  for 492  
 423 vortex events (Figure 8 of Murdoch et al., 2021), all of which would have generated magnetic

424 signals too small to be resolvable by the IFG (Figure 8). The ground tilt required to cause a  
 425 measured magnetic signal of 1 nT is  $\sim 0.03^\circ$ , much larger than the expected or measured ground  
 426 tilt values, and we therefore exclude this mechanism as the cause for magnetic signatures during  
 427 pressure drops.  
 428



429  
 430

431 **Figure 8.** Expected change in the measured magnetic field strength ( $\Delta B$ ) due to ground tilting of  
 432 the lander (rotation around a horizontal direction, Section 3.2.1) and wind-induced lander tilt  
 433 (Section 3.2.2). The reported terrestrial ground tilt (order of magnitude) from Lorenz et al.  
 434 (2015) with the associated predicted  $\Delta B$  is shown (orange star), as are the 66 predicted wind-  
 435 induced tilts at the time of high- $\text{SNR}_\sigma$  pressure drops (gray) with the maximum (25.0 m/s wind  
 436 speed; see section 3.2.2) highlighted in green. Histogram shows ground tilts measured by  
 437 InSight's seismometer (Murdoch et al., 2021).  
 438

439

### 3.2.2 Wind-Induced Lander Tilt

440 Another possibility is that the lander itself is slightly tilted due to wind loads. Considering, for  
 441 purposes of exposition, only the drag force on the side of the lander, the moment of this force  
 442 must be reacted against by the forces on the feet. The feet on the downwind side of the lander  
 443 place a stronger load on the surface than on the upwind side, and if the ground deforms  
 444 elastically to provide these different forces, the lander tilts slightly away from the wind. These  
 445 elastic loads on the ground caused by lander drag and lift are a significant source of noise for the  
 446 seismometer (e.g. Murdoch et al., 2017), even on the ground a meter or two from the lander. For  
 447 a deck-mounted instrument, such as the magnetometer, (and in the first days of the landed  
 448 mission the seismometer), the compliance of the deck to lander wind loads in part results from  
 449 elastic elements in the landing gear. The transfer function of wind speed to deck movement was  
 450 estimated by Panning et al. (2020) to be  $2.1 \times 10^{-7} \text{ (m/s}^2\text{)}/\text{(m/s)}^2$ . We can crudely estimate the  
 451 lander tilt as being this quantity divided by local gravity  $3.7 \text{ (m/s}^2\text{)}$  – in practice the lander tilt  
 452 will depend on the wind direction with respect to the lander feet. For our 66 resolvable events,  
 453 the maximum windspeeds during the pressure drops range from 3.6 to 25.0 m/s. Thus, for a

454 maximum gust of 26.5 m/s associated with a dust devil, the tilt is  $\sim 25.0^2 \times 2.1 \times 10^{-7} / 3.7 = 3.6 \times$   
 455  $10^{-5}$  radians or  $0.002^\circ$ . Per the foregoing discussion and computations of  $\Delta B$  from tilts, such a  
 456 lander tilt can cause an apparent field change of 0.07 nT (Figure 8), and windspeeds would have  
 457 to reach  $\sim 95$  m/s to cause the observed signals of  $\Delta B \sim 1$  nT. Therefore, while wind-induced  
 458 lander tilt can affect IFG measurements, to date, windspeeds are not sufficiently large to be the  
 459 only source of the observed magnetic signals.

460

### 461 3.3 Triboelectric Effects

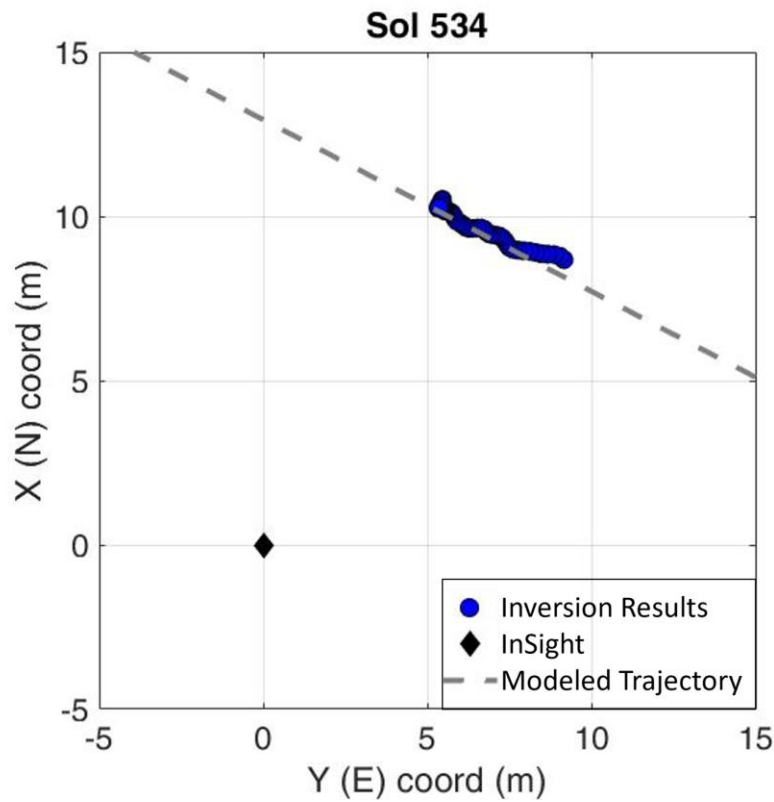
462 A magnetic signal could also be generated by swirling charged dust grains entrained in the DD.  
 463 These grains may become electrically charged via triboelectric effects (contact electrification) in  
 464 which collisions will charge the particles, and a characteristic charge-to-mass ratio develops  
 465 (Farrell et al., 2004). This electrification, coupled with the differential movement of particles  
 466 based on their mass, leads to a magnetic dipole moment and an electric field with an associated  
 467 magnetic field emission (see Figure 1 in Jackson & Farrell, 2006). The spiraling motion of these  
 468 charged grains in cyclostrophic balance (in which the inward pressure gradient force balances the  
 469 outward centripetal force) can be modeled as current loops or a solenoid (Houser et al., 2003;  
 470 Lorenz, 2016). In this approximation, a DD with fixed parameters would produce a stable  
 471 magnetic field (see Figure 4 in Houser, Farrell, & Metzger, 2003). However, DDs have  
 472 constantly fluctuating cross-sectional areas, velocities, and inhomogeneous densities which  
 473 would result in dynamic magnetic fields (Farrell et al., 2004; Farrell et al., 2006; Lorenz, 2016).  
 474 Variations on this model have been invoked to explain the two terrestrial measurements of DD  
 475 magnetic signals (Farrell et al., 2004; Kurgansky et al., 2007), the largest of which was  $\sim 0.1$  nT  
 476 (Farrell et al., 2004). Using this approximation, a large dust devil passing with a high density of  
 477 charged dust grains could be observed by InSight as a quasi-steady magnetic field mostly in the  
 478 vertical direction ( $B_z$  in the lander level frame), possibly with a horizontal field component  
 479 generated by azimuthal asymmetries, such as multiple vortex cores (Lorenz, 2016).

480

481 Recall that no DDs have been detected by InSight's cameras, and only a handful of faint shadows  
 482 on the solar panels have been detected (Lorenz et al., 2020). Furthermore, Jackson et al. (2021)  
 483 reported a maximum optical depth of  $\tau \sim 0.01$  from InSight's cameras at the times of the dustless  
 484 vortices. Therefore, a dust-filled vortex would exceed this value of  $\tau$ . We explore whether an as-  
 485 yet unobserved vortex containing lofted dust could produce signals in the magnetic field. We  
 486 consider the case of a 10 m diameter vortex with a dusty annulus, such that the dust content is  
 487 equivalent to a layer of dust around the perimeter of the vortex that is one particle thick. Thus, the  
 488 effective area of dust is equal to the circumference of the DD multiplied by the diameter of the  
 489 dust grains. Assuming a diameter of  $2 \mu\text{m}$  for dust grains, with a grain density  $2700 \text{ kg/m}^3$ , the  
 490 mass density per meter height,  $\rho_M$ , is  $\sim 0.17 \text{ kg/m}$ . In reality, the dust is spread over a larger cross-  
 491 sectional area, for an annulus of width 1 m in a 10 m diameter vortex, this would correspond to a  
 492 number density of dust grains of  $\sim 3 \times 10^{-12} \text{ m}^{-3}$ . We further assume that dust has a charge-to-mass  
 493 ratio,  $Q/m$ , of  $10^{-6} \text{ C/kg}$  (Mendez Harper et al. 2017), the devil rotates once per second  
 494 (corresponding to a wall circumferential speed,  $v_w$ , of  $10\pi \text{ m/s}$ , typical of intense vortices (Balme  
 495 & Greeley, 2006) and at the upper limit as reported for InSight's vortex catalog by Lorenz et al.  
 496 (2021)). This corresponds to  $\rho_M * Q/m * v_w \sim 5.3 \mu\text{A}$  of current loop per meter height. The  
 497 solenoidal vertical magnetic field  $B$  inside the devil is then  $B = \mu_0 * \rho_M * Q/m * v_w = 6.7 \times 10^{-3} \text{ nT}$ ,  
 498 where  $\mu_0 = 4\pi 10^{-7} \text{ Tm/A}$  is the magnetic permeability of free space.

499

500 To consider this calculation in the context of our most plausible candidate magnetic signals  
 501 (Section 2.3), we examined the 4.0 Pa convective vortex on Sol 534 (Figure 4A) to obtain  
 502 estimates for the event's diameter, trajectory, and miss-distance. We applied the method of  
 503 Murdoch et al. (2021) that uses the simultaneous pressure and seismic measurements of  
 504 convective to place constraints on vortex properties and allow reconstruction of their trajectories.  
 505 The wind speed data (Supplementary Figure 2) shows an increase but no drop at the point of  
 506 closest approach which would be expected if the eye of the vortex passed directly over the  
 507 InSight lander. Furthermore, the absence of a sharp change in wind direction supports the  
 508 inference that InSight is not inside the vortex. The pressure data were fit using the model  
 509 described in Ellehoj et al. (2010), yielding a slightly different FWHM (11.9s) from the gaussian  
 510 fit (14.4s FWHM) described in section 2.2. Assuming that the advection speed is the mean  
 511 background wind speed of 1.9 m/s, the vortex diameter is  $\sim 23$  m (background wind  
 512 speed\*pressure drop FWHM) (Murdoch et al., 2021). Using seismic data (Supplementary Figure  
 513 2), the trajectory of the vortex is found to be in the NE direction during the full encounter, with a  
 514 closest approach at a distance of  $\sim 11.5$  m (Figure 9). The seismic and pressure signals from the  
 515 predicted trajectory were then modeled and compared with the data (Supplementary Figure 3).  
 516 Given the close proximity of the event(s), the direct ground motion has also been included when  
 517 generating the synthetic data (see Murdoch et al., 2017 for details). The results show good  
 518 agreement (Supplementary Figure 3), supporting our trajectory estimate. We note that the  
 519 proximity of the vortex (the vortex wall just grazing the lander) puts it at the limit of the  
 520 modeling approach which assumes a far field point source. We attempted a similar analysis for  
 521 the event on sol 652; however, the simple point source model did not fit the seismic observations  
 522 well, likely due to the close approach of the vortex.



525 **Figure 9.** Trajectory of the 4.0 Pa convective vortex on Sol 534 (Figure 4A). The grey dashed  
 526 line modeled trajectory is the straight line fit to the pressure and seismic data inversion results in  
 527 blue.

528

529 We substitute the derived diameter of this close approach event into the triboelectric model  
 530 calculation above and the resulting DD could generate a magnetic field of  $\sim 0.016$  nT. Therefore,  
 531 for this candidate event, the magnetic signal is still an order of magnitude too small to generate  
 532 the observed signal of  $\sim 0.3$  nT.

533

534 The following question arises: Can triboelectric effects cause a resolvable signature? To answer  
 535 this question, we explore the extent to which the parameters above - the DD diameter, wall  
 536 circumferential speed,  $v_w$ , dust grain diameter, and the charge-to-mass ratio,  $Q/m$  - could  
 537 reasonably be varied. The predicted magnetic field scales linearly with each of these parameters  
 538 and an order of magnitude increase in total could explain the observed signal amplitudes.  
 539 Jackson et al. (2021) used models of the pressure and wind speed profiles for their catalog of  
 540 InSight's vortices to infer intrinsic vortex parameters for a subset of events during which the  
 541 inferred closest approach distance was within a vortex diameter from the lander. While their  
 542 most extreme value for DD eyewall velocity of  $\sim 37$  m/s is similar to our  $v_w$ , they report  
 543 diameters reaching hundreds of meters (a maximum of  $\sim 517$  m). Clearly this is not the case for  
 544 the event on sol 534, for which we can estimate the vortex diameter, but other vortices could be  
 545 larger. Furthermore, our estimate for dust grain diameter ( $2 \mu\text{m}$ ) is in line with observations for  
 546 fine atmospheric dust on Mars (Pollack et al., 1995); however, spectral observations during the  
 547 2018 dust storm by the Curiosity rover showed dust enhancement by particles  $\sim 3$  times the  
 548 typical size ( $\sim 8 \mu\text{m}$ ) (Lemmon et al. 2019). Terrestrial measurements of dust devil mean grain  
 549 diameter values range from  $\sim 90$ - $100 \mu\text{m}$  decreasing with height (Raack et al. 2018), although the  
 550 thin Martian atmosphere may poorly suspend larger grains comparatively (Merrison et al. 2004).  
 551 Dust grain diameters lifted by a large DD, especially closer to the ground, could therefore be  $\sim 5$   
 552 times larger than we assume. For a constant optical depth, a dust devil comprised of larger grains  
 553 could allow for a larger signal as their area increases by the square of the grain radius while their  
 554 mass (and therefore charge density) increases by the grain radius cubed. Alternatively, if large  
 555 grains are not lifted far from the ground, a shallow toroid of swirling sand rather than a canonical  
 556 DD may yield the observed magnetic field signature signals. Terrestrial measurements for  $Q/m$   
 557 of sand and volcanic ash can reach maximum values of  $10^{-5}$  C/kg (Tian-Li et al., 2014), while  
 558 experiments of the Mars dust simulant JSC Mars-1 tribocharged against stainless steel and  
 559 Teflon have generated  $Q/m$  ratios much larger (Sharma et al. 2008). The dust concentration could  
 560 also be higher. In conclusion, higher values for dust devil diameter, dust grain diameter, or  $Q/m$   
 561 are plausible and could lead to triboelectrically-driven magnetic fields on the order of 0.1 nT  
 562 (Section 2.3), for a close DD trajectory.

563

564

### 565 3.4 Synthesis

566 We examined several mechanisms that could lead to magnetic signatures during pressure drops.  
 567 Our investigation of solar array current drops at times of resolvable magnetic signatures shows  
 568 that SAC changes are present both with and without magnetic signals (and vice versa) and are  
 569 therefore not the sole contributor to IFG signals. Furthermore, tilt of either the lander or the  
 570 ground resulting in re-orientation of the IFG with respect to the background crustal field can be

571 ruled out because the expected and measured tilts reported at InSight are too small to create  
572 magnetic signals of resolvable magnitude. Finally, although triboelectric effects are theoretically  
573 possible, the estimates made in Section 3.3 indicate that these are not likely to frequently create  
574 measurable magnetic fields unless the DD has a large diameter, a very close approach distance  
575 and carries sufficient charged dust. A purely solenoidal (i.e. rotationally-symmetric) field from a  
576 vertical dust devil would be a quasi-DC signal – increasing slowly from zero as the devil  
577 approached, reaching a maximum and then declining. Therefore, if the slow approach and signal  
578 generation of a magnetic field-generating vortex was considerably longer than the duration of  
579 our pressure drop, our resolvable event detection methodology may not positively detect it.

580

581 Convective vortices can also be detected by a corresponding rise in temperature with a core  
582 temperature rise of up to 10 K, although elevated temperatures are observed if the sensor enters  
583 the vortex core (Ringrose et al. 2007). Because IFG measurements are sensitive to temperature  
584 fluctuations (Mittelholz et al. 2020, Thorne et al. 2020), IFG sensor temperature data for all  
585 events in Figure 4 were investigated, and we found no corresponding temperature signals. In the  
586 case of the event on sol 534 for which we have a derived trajectory, this is consistent with a dust  
587 devil that passed close to but not directly over the lander. Furthermore, as shown in Joy et al.  
588 (2019), if temperature were the cause, then we should see similar relative changes in the 3  
589 components from one event to another, whose amplitude just depended on the amplitude of the  
590 thermal perturbation. This is not the case as can be seen from Figures 4 and 7, e.g. in Figures 4A  
591 and 4B, even the signs of the perturbations to  $B_x$  and  $B_y$  are opposite. We thus rule out that  
592 unmodeled temperature perturbations are responsible for the IFG signals

593

594 Although InSight has recorded a large number of pressure drops, there are relatively few with  
595 resolvable magnetic signatures. Only 7.7% of pressure drops larger than 1 Pa correlate in time  
596 with such magnetic signatures, which is only 0.6% of all recorded pressure drops. Furthermore,  
597 given the frequency of pressure drops, it is remarkable that no characteristic DD has been  
598 successfully imaged by the ongoing imagery surveys. While DD tracks have been observed  
599 around the lander (Perrin et al., 2021), there have been no images of lofted columnar dust at the  
600 InSight landing site to date. This is in stark contrast to other martian missions (Lorenz, Spiga, et  
601 al., 2021). The dearth of imaged DDs and low proportion of observed magnetic signatures  
602 despite numerous measured pressure drops is consistent with a small proportion of convective  
603 vortices carrying lofted dust. In most cases with minimal entrained dust solar array currents are  
604 largely unaffected with little to no contribution to IFG signals, and triboelectric charging likely  
605 does not occur or is minimal.

606

607 The local environment at InSight may be a contributing factor to the lack of dust lifting  
608 necessary for DD development. While aeolian activity has been reported at InSight including  
609 surface creep of particulate and dust removal (Charalambous et al., 2021; Baker et al. 2021), and  
610 dust deposition occurs, including critically upon the solar panels (Lorenz, Lemmon, & Maki,  
611 2021), the requirements for saltation leading to DDs may be rarely met. Lorenz, Lemmon, &  
612 Maki (2021) estimate that the dust lifting pressure drop threshold at InSight is roughly between  
613 4 and 10 Pa, though they also acknowledge much higher dust lifting thresholds from other Mars  
614 missions (6-40 Pa based on data from Pathfinder, Phoenix, and Spirit) and terrestrial  
615 observations (20-80 Pa). Furthermore, based on the non-detection of DD's by the InSight  
616 camera, Jackson et al. (2021) calculated a localized dust lifting threshold of ~7 Pa. As shown in

617 Figure 1, such a threshold would exclude most of the pressure drop events examined in this  
618 study, even if the observed pressure drop is a lower limit for the actual central pressure drop. By  
619 comparing vortex encounters parameters with advective wind speeds Jackson et al. (2021) found  
620 evidence that high wind speeds at InSight may have led to the suppression of dust lifting for the  
621 most vigorous vortices.

622

#### 623 4 Conclusions

624 We analyzed the magnetic field at InSight at times of pressure drops during the first year of  
625 observations to identify if pressure drops might correlate with a magnetic response. We found  
626 coincident magnetic field signals, albeit rarely, as 7.7% of data during drops greater than 1 Pa  
627 had a magnetic signal in any component. The mechanism that causes these signals is as yet  
628 inconclusive, but is not indicative of ground or lander tilting in response to the localized pressure  
629 drop (Murdoch et al., 2021). While dust laden convective vortices in close approach could  
630 explain our resolvable events, especially those discussed in Section 2.3, our analysis indicates  
631 that in general the magnetic signals expected from DDs are too small to be detected. In  
632 summary, our observations show (a) no observed magnetic field signal for the vast majority of  
633 pressure drops and (b) a few pressure drops, ( $\sim 9$ , i.e.  $< 1\%$  of the overall population of pressure  
634 drops  $> 1\text{ Pa}$ ) with magnetic field signals  $< \sim 1\text{ nT}$ , possibly corresponding to more dust laden  
635 vortices that would have had to have passed close to the lander. Modeling of pressure and  
636 seismic data for one of these 9 pressure drops on sol 534, suggests a vortex diameter of  $\sim 23\text{ m}$ ,  
637 and indicates that nominal parameters for dust grain diameter, charge-to mass density, and a dust  
638 content corresponding to  $\sim 3 \times 10^{-12}$  particles per  $\text{m}^3$ , underpredicts the observed magnetic field  
639 signal by an order of magnitude. The magnetic field signal depends linearly on all these  
640 parameters, as well as on the dust-devil diameter and thus if triboelectric effects are indeed the  
641 cause of the full signal during these few pressure drop events, larger values for one or more of  
642 the dust parameters are required. The remaining population of events that appear to have an  
643 enhanced magnetic signal (high SNR events,  $\sim 5\%$  of the pressure drops  $> 1\text{ Pa}$ ) compared with  
644 the time intervals immediately preceding and after the pressure drop, are more difficult to assess:  
645 some of these comprise very small signals ( $< \sim 0.1\text{ nT}$ ) that could potentially be consistent with  
646 DD related signatures, however larger signals, especially those  $> 1\text{ nT}$  would require DD  
647 parameters outside the limit of current studies

648

649 A larger number of events with 2 Hz IFG data and 0.2 Hz solar array current data could  
650 strengthen this investigation, as would an unambiguous event detection by InSight's cameras to  
651 provide a positive control. Analysis of the coincidence of solar array current signals and IFG  
652 signals is limited by the intermittent nature of the SAC data. However, the DD solar panel  
653 cleaning events which were anticipated have not yet transpired and the power constraints during  
654 the current winter season resulting from the accumulation of dust on the solar panels have led to  
655 IFG not collecting continuous data since late 2020. Further martian missions with meteorological  
656 instruments and magnetometers, such as China's Tianwen Zhurong lander, could also address  
657 the magnetic signals associated with pressure drops and DDs (Du et al., 2020), as could  
658 continued terrestrial studies like those of the MATADOR campaign in the Arizona desert (Renno  
659 et al., 2004; Farrell et al., 2004). Further understanding of DDs can help explain why they have  
660 not yet been imaged at the InSight landing site, while all other Mars surface missions with visual  
661 cameras have imaged several cases of dust devils (Ferri et al., 2003, Ellehoj et al., 2010).

662

663 **Acknowledgments**

664  
 665 We acknowledge NASA, CNES, their partner agencies and Institutions (UKSA, SSO, DLR, JPL,  
 666 IPGP-CNRS, ETHZ, IC, MPS-MPG) and flight operations team at JPL, SIS-MOC (SEIS on  
 667 Mars Operations Center) and MSDS (Mars SEIS Data Service). We acknowledge support from  
 668 the Natural Sciences and Engineering Research Council of Canada (S.T, C.L.J.), the Canadian  
 669 Space Agency and the InSight Mission (C.L.J.), CNES in the frame of the InSight mission (A.S,  
 670 B.L.), as well as ETH 19-2 FEL-34 and funding through the Harvard Daly Fellowship (A.M.).  
 671 All InSight data used in this study are publicly available in the Planetary Data System: InSight  
 672 IFG calibrated data <https://doi.org/10.17189/1519202> and Calibration data  
 673 <https://doi.org/10.17189/1510486>. This paper is InSight Contribution Number, ICN 231.

674  
675 **References**

- 676 Atreya, S. K., Wong, A. S., Renno, N. O., Farrell, W. M., Delory, G. T., Sentman, D. D., ...  
 677 Catling, D. C. (2006). Oxidant enhancement in Martian dust devils and storms: Implications  
 678 for life and habitability. *Astrobiology*, 6(3), 439–450. <https://doi.org/10.1089/ast.2006.6.439>
- 679 Baker, M., Newman, C., Charalambous, C., Golombek, M., Spiga, A., Banfield, D., et al. (2021).  
 680 Vortex-dominated aeolian activity at InSight's landing site, Part 2: Local meteorology,  
 681 transport dynamics, and model analysis. *Journal of Geophysical Research: Planets*, 126,  
 682 e2020JE006514. <https://doi.org/10.1029/2020JE006514>
- 683 Balme, M., & Greeley, R. (2006). Dust devils on Earth and Mars. *Reviews of Geophysics*, 44(3),  
 684 RG3003. <https://doi.org/10.1029/2005RG000188>
- 685 Banerdt, W. B., Smrekar, S. E., Banfield, D., Giardini, D., Golombek, M., Johnson, C. L., ...  
 686 Wieczorek, M. (2020). Initial results from the InSight mission on Mars. *Nature Geoscience*.  
 687 <https://doi.org/10.1038/s41561-020-0544-y>
- 688 Bo, T. L., Zhang, H., & Zheng, X. J. (2014). Charge-to-mass ratio of saltating particles in wind-  
 689 blown sand. *Scientific Reports*, 4. <https://doi.org/10.1038/srep05590>
- 690  
 691 Banfield, D, Rodriguez-Manfredi, J. A., Russell, C. T., Rowe, K. M., Leneman, D., Lai, H. R.,  
 692 ... Team, T. T. (2018). InSight Auxiliary Payload Sensor Suite (APSS). *Space Science*  
 693 *Reviews*, 215(1), 4. <https://doi.org/10.1007/s11214-018-0570-x>
- 694 Banfield, D., Spiga, A., Newman, C., Forget, F., Lemmon, M., Lorenz, R., ... Banerdt, W. B.  
 695 (2020). The atmosphere of Mars as observed by InSight. *Nature Geoscience*, 13(3), 190–  
 696 198. <https://doi.org/10.1038/s41561-020-0534-0>
- 697 Charalambous, C., McClean J., B., Baker, M., Pike, W. T., Golombek, M., Lemmon, M., ...  
 698 Banerdt, W. B. (2021). Vortex-dominated aeolian activity at InSight's landing site, Part 1:  
 699 Multi-instrument Observations, Analysis and Implications. *Journal of Geophysical*  
 700 *Research: Planets*. <https://doi.org/10.1029/2020je006757>

- 701 Chatain, A. and Spiga, A. and the InSight team: Seasonal variability of Mars atmospheric  
702 turbulence studied from InSight high-frequency pressure measurements, *European*  
703 *Planetary Science Congress 2021*, online, 13–24 Sep 2021, EPSC2021-290,  
704 <https://doi.org/10.5194/epsc2021-290>, 2021.
- 705 Du, A. M., Zhang, Y., Li, H. Y., Qiao, D. H., Yi, Z., Zhang, T. L., ... Dai, J. L. (2020). The  
706 Chinese Mars ROVER Fluxgate Magnetometers. *Space Science Reviews*.  
707 <https://doi.org/10.1007/s11214-020-00766-8>
- 708 Ellehoj M. D., Gunnlaugsson H. P., Taylor P. A. et al. (2010). Convective vortices and dust  
709 devils at the Phoenix Mars mission landing site. *Journal of Geophysical Research*.  
710 <https://doi.org/10.1029/2009JE003413>
- 711 Farrell, W. M., Smith, P. H., Delory, G. T., Hillard, G. B., Marshall, J. R., Catling, D., ...  
712 Johnson, B. (2004). Electric and magnetic signatures of dust devils from the 2000-2001  
713 MATADOR desert tests. *Journal of Geophysical Research E: Planets*, 109(3).  
714 <https://doi.org/10.1029/2003je002088>
- 715 Farrell, William M., Marshall, J. R., Cummer, S. A., Delory, G. T., & Desch, M. D. (2006). A  
716 model of the ULF magnetic and electric field generated from a dust devil. *Journal of*  
717 *Geophysical Research E: Planets*, 111(11), E11004. <https://doi.org/10.1029/2006JE002689>
- 718 Fenton, L. K., & Lorenz, R. (2015). Dust devil height and spacing with relation to the Martian  
719 planetary boundary layer thickness. *Icarus*. <https://doi.org/10.1016/j.icarus.2015.07.028>
- 720 Ferri F., Smith P. H., Lemmon, M., Renno, N. O. (2003) Dust devils as observed by Mars  
721 Pathfinder. *Journal of Geophysical Research*. <https://doi.org/10.1029/2000JE001421>
- 722 Harrison, R. G., Barth, E., Esposito, F., Merrison, J., Montmessin, F., Aplin, K. L., ...  
723 Zimmerman, M. (2016). Applications of Electrified Dust and Dust Devil Electrodynamics  
724 to Martian Atmospheric Electricity. *Space Science Reviews*, Vol. 203, pp. 299–345.  
725 <https://doi.org/10.1007/s11214-016-0241-8>
- 726 Houser, J. G., Farrell, W. M., & Metzger, S. M. (2003). ULF and ELF magnetic activity from a  
727 terrestrial dust devil. *Geophysical Research Letters*, 30(1).  
728 <https://doi.org/10.1029/2001GL014144>
- 729 Jackson, T. L., & Farrell, W. M. (2006). Electrostatic fields in dust devils: An analog to Mars.  
730 *IEEE Transactions on Geoscience and Remote Sensing*, 44(10), 2942–2949.  
731 <https://doi.org/10.1109/TGRS.2006.875785>
- 732 Jackson, B., Crevier, J., Szurgot, M., Battin, R., Clement, P., Rodriguez, S. (2021) Inferring  
733 Vortex and Dust Devil Statistics from InSight. *The Planetary Science Journal*, 2 206.  
734 <https://doi.org/10.3847/PSJ/ac260d>
- 735 Johnson, C. L., Mittelholz, A., Langlais, B., Russell, C. T., Ansan, V., Banfield, D., ... Banerdt,

- 736 W. B. (2020). Crustal and time-varying magnetic fields at the InSight landing site on Mars.  
737 *Nature Geoscience*, 13(3), 199–204. <https://doi.org/10.1038/s41561-020-0537-x>
- 738 Joy, S. P., Mafi, J. N., & Slavney, S. (2019). Interior Exploration Using Seismic Investigations,  
739 Geodesy, and Heat Transport (InSight) Mission Insight Fluxgate Magnetometer (IFG) PDS  
740 Archive Software Interface Specification. *urn:nasa:pds:insight-ifg-mars:document:insight-*  
741 *ifg-sis*.
- 742 Kahre, M. A., Murphy, J. R., & Haberle, R. M. (2006). Modelling the Martian dust cycle and  
743 surface dust reservoirs with the NASA Ames general circulation model. *Journal of*  
744 *Geophysical Research E: Planets*. <https://doi.org/10.1029/2005JE002588>
- 745 Kok, J. F., and Renno, N. O. (2009), Electrification of wind-blown sand on Mars and its  
746 implications for atmospheric chemistry, *Geophys. Res. Lett.*, 36, L05202,  
747 [doi:10.1029/2008GL036691](https://doi.org/10.1029/2008GL036691).
- 748 Kurgansky, M. V, Baez, L., & Ovalle, E. M. (2007). A simple model of the magnetic emission  
749 from a dust devil. *Journal of Geophysical Research E: Planets*, 112(11), 11008.  
750 <https://doi.org/10.1029/2007JE002952>
- 751 Lemmon, M. T., Guzewich, S. D., McConnochie, T., de Vicente-Retortillo, A., Martínez, G.,  
752 Smith, M. D., ... Jacob, S. (2019). Large Dust Aerosol Sizes Seen During the 2018 Martian  
753 Global Dust Event by the Curiosity Rover. *Geophysical Research Letters*, 46(16).  
754 <https://doi.org/10.1029/2019GL084407>  
755
- 756 Lognonné, P., Banerdt, W. B., Pike, W. T., Giardini, D., Christensen, U., Garcia, R. F., ...  
757 Zweifel, P. (2020). Constraints on the shallow elastic and anelastic structure of Mars from  
758 InSight seismic data. *Nature Geoscience*. <https://doi.org/10.1038/s41561-020-0536-y>
- 759 Lorenz, R. D. (2016). Heuristic estimation of dust devil vortex parameters and trajectories from  
760 single-station meteorological observations: Application to InSight at Mars. *Icarus*, 271,  
761 326–337. <https://doi.org/10.1016/j.icarus.2016.02.001>
- 762 Lorenz, R. D., & Jackson, B. K. (2015). Dust devils and dustless vortices on a desert playa  
763 observed with surface pressure and solar flux logging. *GeoResJ*.  
764 <https://doi.org/10.1016/j.grj.2014.11.002>
- 765 Lorenz, R. D., Kedar, S., Murdoch, N., Lognonné, P., Kawamura, T., Mimoun, D., & Banerdt,  
766 W. B. (2015). Seismometer detection of dust devil vortices by ground tilt. *Bulletin of the*  
767 *Seismological Society of America*, 105(6), 3015–3023. <https://doi.org/10.1785/0120150133>
- 768 Lorenz, R. D., Lemmon, M. T., & Maki, J. (2021). First mars year of observations with the  
769 InSight solar arrays: Winds, dust devil shadows, and dust accumulation. *Icarus*.  
770 <https://doi.org/10.1016/j.icarus.2021.114468>

- 771 Lorenz, R. D., Lemmon, M. T., Maki, J., Banfield, D., Spiga, A., Charalambous, C., ... Banerdt,  
 772 W. B. (2020). Scientific Observations With the InSight Solar Arrays: Dust, Clouds, and  
 773 Eclipses on Mars. *Earth and Space Science*. <https://doi.org/10.1029/2019EA000992>
- 774 Lorenz, R. D., & Reiss, D. (2015). Solar panel clearing events, dust devil tracks, and in-situ  
 775 vortex detections on Mars. *Icarus*, 248, 162–164.  
 776 <https://doi.org/10.1016/J.ICARUS.2014.10.034>
- 777 Lorenz, R. D., Spiga, A., Lognonné, P., Plasman, M., Newman, C. E., & Charalambous, C.  
 778 (2021). The whirlwinds of Elysium: A catalog and meteorological characteristics of “dust  
 779 devil” vortices observed by InSight on Mars. *Icarus*, 355, 114119.  
 780 <https://doi.org/10.1016/j.icarus.2020.114119>
- 781 Méndez Harper, J., McDonald, G., Dufek, J. Malaska, M. J., Burr D. M., Hayes, A. G.,  
 782 McAdams, J., Wray, J. J. (2017). Electrification of sand on Titan and its influence on  
 783 sediment transport. *Nature Geoscience* 10, 260–265 <https://doi.org/10.1038/ngeo2921>
- 784 Merrison, J. P., Bertelsen, P., Frandsen, C., Gunnlaugsson, P., Knudsen, J. M., Lunt, S., ...  
 785 Uggerhøj, E. (2002). Simulation of the Martian dust aerosol at low wind speeds. *Journal of*  
 786 *Geophysical Research E: Planets*, 107(12). <https://doi.org/10.1029/2001je001807>  
 787
- 788 Mittelholz, A., Johnson, C. L., Thorne, S. N., Joy, S., Barrett, E., Fillingim, M. O., ... Banerdt,  
 789 W. B. (2020). The Origin of Observed Magnetic Variability for a Sol on Mars From  
 790 InSight. *Journal of Geophysical Research: Planets*, 125(9).  
 791 <https://doi.org/10.1029/2020JE006505>
- 792 Mittelholz, A., Johnson, C. L., Thorne, S. N., Yau, V., Joy, S., Barrett, E., ... Banerdt, W. B.  
 793 (2021). Magnetic Variations of a Sol Observed Over a Year on Mars with InSight. Lunar  
 794 and Planetary Science Conference. *LPI Contributions* 2548.  
 795 <https://www.hou.usra.edu/meetings/lpsc2021/pdf/1941.pdf>
- 796 Murdoch, N., Spiga, A., Lorenz, R., Garcia, R. F., Perrin, C., Widmer-Schmidrig, R., ... Banerdt,  
 797 W. B. (2021). Constraining Martian Regolith and Vortex Parameters From Combined  
 798 Seismic and Meteorological Measurements. *Journal of Geophysical Research: Planets*.  
 799 <https://doi.org/10.1029/2020JE006410>
- 800 Murdoch, N., Mimoun, D., Garcia, R. F., Rapin, W., Kawamura, T., Lognonné, P., ... Banerdt,  
 801 W. B. (2017). Evaluating the Wind-Induced Mechanical Noise on the InSight  
 802 Seismometers. *Space Science Reviews*. <https://doi.org/10.1007/s11214-016-0311-y>
- 803 Panning, M. P., Pike, W. T., Lognonné, P., Banerdt, W. B., Murdoch, N., Banfield, D., ...  
 804 Warren, T. (2020). On-Deck Seismology: Lessons from InSight for Future Planetary  
 805 Seismology. *Journal of Geophysical Research: Planets*.  
 806 <https://doi.org/10.1029/2019JE006353>

- 807 Pollack, J. B., Ockert-Bell, M. E., & Shepard, M. K. (1995). Viking Lander image analysis of  
 808 Martian atmospheric dust. *Journal of Geophysical Research*, 100(E3).  
 809 <https://doi.org/10.1029/94JE02640>  
 810
- 811 Raack, J., Reiss, D., Balme, M. R., Taj-Eddine, K., & Ori, G. G. (2018). In Situ Sampling of  
 812 Relative Dust Devil Particle Loads and Their Vertical Grain Size Distributions.  
 813 *Astrobiology*, 18(10). <https://doi.org/10.1089/ast.2016.1544>
- 814 Renno, N. O., Abreu, V. J., Koch, J., Smith, P. H., Hartogensis, O. K., De Bruin, H. A., Burose,  
 815 D., Delory, G. T., Farrell, W. M., Watts, C. J., & Garatuza, J. (2004). MATADOR 2002: A  
 816 pilot field experiment on convective plumes and dust devils. *Journal of Geophysical*  
 817 *Research: Planets*, 109(E7), E07001. <https://doi.org/10.1029/2003JE002219>
- 818 Ringrose, T. J., Patel, M. R., Towner, M. C., Balme, M., Metzger, S. M., & Zarnecki, J. C.  
 819 (2007). The meteorological signatures of dust devils on Mars. *Planetary and Space Science*,  
 820 55(14). <https://doi.org/10.1016/j.pss.2007.07.002>  
 821
- 822 Sharma, R., Clark, D. W., Srirama, P. K., & Mazumder, M. K. (2008). Tribocharging  
 823 characteristics of the Mars dust simulant (JSC Mars-1). *IEEE Transactions on Industry*  
 824 *Applications*, 44(1). <https://doi.org/10.1109/TIA.2007.912761>  
 825
- 826 Spiga, A., Barth, E., Gu, Z., Hoffmann, F., Ito, J., Jemmett-Smith, B., ... Wei, W. (2016). Large-  
 827 Eddy Simulations of Dust Devils and Convective Vortices. *Space Science Reviews*.  
 828 <https://doi.org/10.1007/s11214-016-0284-x>
- 829 Spiga, A., Murdoch, N., Lorenz, R., Forget, F., Newman, C., Rodriguez, S., ... Banerdt, W. B.  
 830 (2021). A study of daytime convective vortices and turbulence in the Martian planetary  
 831 boundary layer based on half-a-year of InSight atmospheric measurements and large-eddy  
 832 simulations. *Journal of Geophysical Research: Planets*, 126, e2020JE006511.  
 833 <https://doi.org/10.1029/2020JE006511>
- 834 Stähler, S. C., Widmer-Schmidrig, R., Scholz, J.-R., van Driel, M., Mittelholz, A., Hurst, K., ...  
 835 et al. (2020). Geophysical observations of Phobos transits by InSight. *Earth and Space*  
 836 *Science Open Archive*, 15. <https://doi.org/10.1002/essoar.10503257.1>
- 837 Stott, A. E., Garcia, R. F., Pinot, B., Murdoch, N., Mimoun, D., Spiga, A., Banfield, D., Navarro,  
 838 S., Mora-Sotomayor, L., Charalambous, C., Pike, W. T., Lognonné, P., and Horleston, A.:  
 839 Atmospherically driven ground motion at InSight: a machine learning perspective, *EGU*  
 840 *General Assembly 2021*, online, 19–30 Apr 2021, EGU21-12344,  
 841 <https://doi.org/10.5194/egusphere-egu21-12344>, 2021
- 842 Thomas, P., & Gierasch, P. J. (1985). Dust devils on Mars. *Science*.  
 843 <https://doi.org/10.1126/science.230.4722.175>

844 Thorne, S. N., Mittelholz, A., Johnson, C. L., Joy, S., Liu, X., Russell, C. T., ... Banerdt, W. B.  
845 (2020). InSight fluxgate magnetometer data calibration assessment and implications. *LPI*  
846 *Contributions* 2089.